



Antipodal focusing of seismic waves observed with the USArray

L. Retailleau, N. M Shapiro, J. Guilbert, M. Campillo, P. Roux

► To cite this version:

L. Retailleau, N. M Shapiro, J. Guilbert, M. Campillo, P. Roux. Antipodal focusing of seismic waves observed with the USArray. *Geophysical Journal International*, 2014, 199 (2), pp.1030-1042. 10.1093/gji/ggu309 . insu-02277353

HAL Id: insu-02277353

<https://insu.hal.science/insu-02277353>

Submitted on 3 Sep 2019

HAL is a multi-disciplinary open access archive for the deposit and dissemination of scientific research documents, whether they are published or not. The documents may come from teaching and research institutions in France or abroad, or from public or private research centers.

L'archive ouverte pluridisciplinaire **HAL**, est destinée au dépôt et à la diffusion de documents scientifiques de niveau recherche, publiés ou non, émanant des établissements d'enseignement et de recherche français ou étrangers, des laboratoires publics ou privés.

Antipodal focusing of seismic waves observed with the USArray

L. Retailleau,^{1,2} N. M. Shapiro,¹ J. Guilbert,² M. Campillo³ and P. Roux³

¹*IPGP, Sorbonne Paris Cité, CNRS (UMS 7154), Paris, France. E-mail: retailleau.lise@gmail.com*

²*CEA/DAM/DIF, F-91297 Arpajon, France*

³*Institut des Sciences de la Terre, CNRS, Université Joseph Fournier, Grenoble, France*

Accepted 2014 August 4. Received 2014 July 25; in original form 2014 May 27

SUMMARY

We present an analysis of the $M_w = 5.3$ earthquake that occurred in the Southeast Indian Ridge on 2010 February 11 using USArray data. The epicentre of this event is antipodal to the USArray, providing us with an opportunity to observe in details the antipodal focusing of seismic waves in space and time. We compare the observed signals with synthetic seismograms computed for a spherically symmetric earth model (PREM). A beamforming analysis is performed over the different seismic phases detected at antipodal distances. Direct spatial snapshots of the signals and the beamforming results show that the focusing is well predicted for the first P -wave phases such as PKP or PP . However, converted phases ($SKSP$, PPS) show a deviation of the energy focusing to the south, likely caused by the Earth's heterogeneity. Focusing of multiple S -wave phases strongly deteriorates and is barely observable.

Key words: Earthquake source observations; Body waves; Wave propagation.

1 INTRODUCTION

Focusing of seismic waves at the antipode of a seismic source has been attracting the attention of seismologists for many reasons. In antipodal regions, seismic phases propagating through the inner core can be observed, providing information about the structure of this deepest part of the Earth (e.g. Butler *et al.* 1986; Sun & Song 2002; Niu & Chen 2008). Antipodal energy focusing is also believed to play an important role during planetary-scale impacts (e.g. Meschede *et al.* 2011). One can thus consider the antipode as a ‘collector’ of seismic-wave information (Rial 1978) where the waves propagating along different paths from all possible directions meet. At the antipode the waves concentrate and interfere, containing a global view of the Earth in a reduced area.

With modern numerical methods, the antipodal focusing of seismic waves can be studied theoretically in spherically symmetrical and heterogeneous Earth's models (e.g. Meschede *et al.* 2011). In contrast, only very few observations of seismic signals recorded at antipodes of real earthquakes have been reported (e.g. Rial 1978; Rial & Cormier 1980; Poupinet *et al.* 1993; Sun & Song 2002; Cormier & Stroujkova 2005; Niu & Chen 2008; Butler & Tsuboi 2010). Furthermore, quantifying the wave-focusing requires comparing observations at several stations located close to the antipode but at different distances from it. Lin & Tsai (2013) showed observation of the waves amplification at the antipode using waveforms reconstructed from seismic noise cross correlation methods.

Rial & Cormier (1980) used records at four stations, with epicentral distances ranging from 166.03° to 179.25° , to observe a clear antipodal amplification of different P phases (except the direct PKIKP wave). The observed waveforms, including their

amplitudes, were found to be very similar to synthetic seismograms computed in spherically symmetrical earth models at the same set of epicentral distances. However, the small number of stations used did not allow these authors to investigate the details of the wave focusing in space.

In this study, we use a $M_w = 5.3$ earthquake that occurred in the Southeast Indian ridge on 2010 February 11. The epicentre of this event was antipodal to the position of the Transportable Array (TA) component of the USArray (Fig. 1a). Therefore, the records of this earthquake by the TA stations provide us with a dense sampling of an antipodal wavefield over an extended area. We use instantaneous spatial snapshots of the observed wavefield and beamforming analysis to study the details of the spatial focusing of different seismic phases. The observations are compared with synthetic seismograms computed in the spherically symmetric earth model PREM (Dziewonski & Anderson 1981) in a period band between 20 and 50 s.

2 DATA

The earthquake of 2010 February 11 occurred in the Indian Ocean east of Amsterdam and St Paul Islands and had a magnitude M_w of 5.3. The earthquake's epicentre was located about 300 km off the Southeast Indian ridge (Fig. 1b) and was antipodal to the region where the USArray transportable network component was operating at that time (Fig. 1a). The moment tensor solution obtained from the global CMT project (Dziewonski & Anderson 1981; Ekström *et al.* 2012) indicates a thrust faulting mechanism with a strong non-double-couple component (Fig. 1). Such mechanism is unusual for

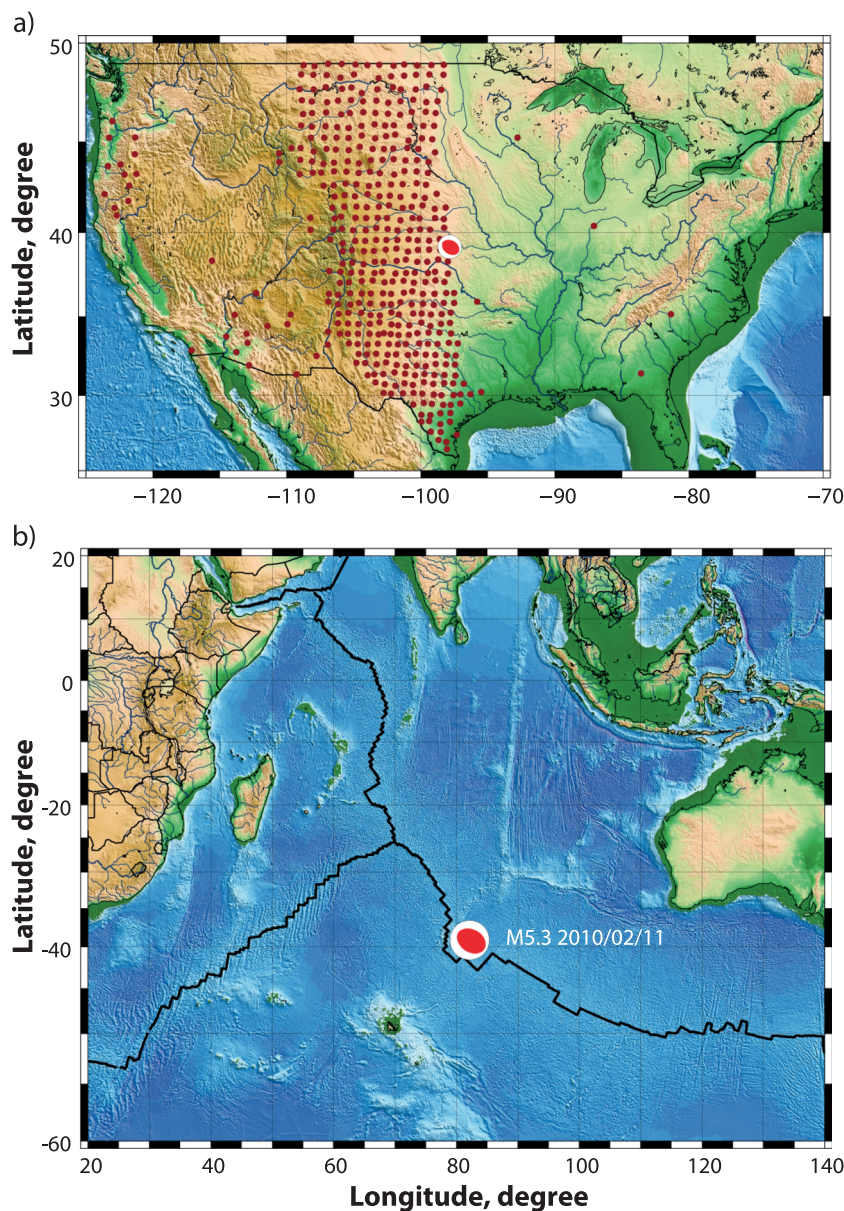


Figure 1. (a) Locations of USArray transportable array stations at the time of study with the location of the earthquake antipode. (b) Location and focal mechanism of the studied earthquake. Black lines indicate Indian Ocean ridges.

a mid-oceanic ridge environment and there is a possibility that it was not well resolved because of the poor station coverage in the southern hemisphere. At the same time, this intraplate event did not occur exactly at the ridge, which might explain the unusual mechanism. For the trust-fault event, all antipodal rays are concentrated near the maximum of the P -wave radiation pattern. We use the records from 411 stations of the USArray. All seismograms were corrected for instrumental responses and filtered with a Butterworth band pass filter between 20 and 50 s. Only the vertical component seismograms are used in this study.

3 ANTIPODAL AMPLIFICATION

Several phases may be detected at the antipode of an earthquake, having travelled through the mantle and core, as shown in Figs 2(a)

and 3. Several phases are clearly observable in Fig. 3, where the signals of the three stations closest to the antipode are plotted. PKP ($PKPab$), PP , $PcPPKP$, PPP , $SKSP$ and PPS show a strong signal-to-noise ratio. $PKIKP$ ($PKPdf$) does not benefit from the amplification and thus is not clearly observable. However, the waveforms at the time of the $PKIKP$ arrival are in phase indicating the signals from tele seismic waves and not a local noise.

Except for $PKIKP$ ($PKPdf$), which travels directly through the crust, mantle and core without any reflection or refraction and arrives at the antipode as an approximately plane wave, all the phases exhibit clear antipodal amplification resulting from the coherent interference of the waves reaching the antipode from all the different azimuths.

To illustrate the antipodal amplification, we compare seismograms recorded at different epicentral distances (Figs 4a and 5a). The signals were averaged in different distance bins to increase the

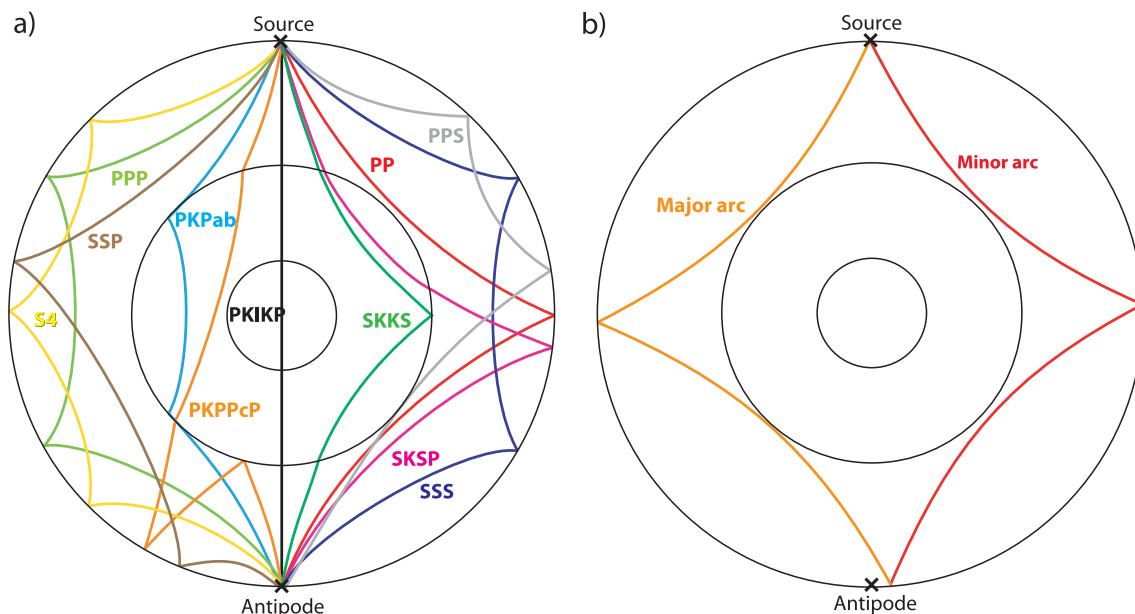


Figure 2. (a) Different seismic phases reaching the antipode of an earthquake. The phases travel through all the azimuth of the Earth. Paths were obtained using TauP path calculator (Crotwell *et al.* 1999) based on the method of Buland & Chapman (1983). (b) Travel paths of the major and minor arc of a phase (here *PP*).

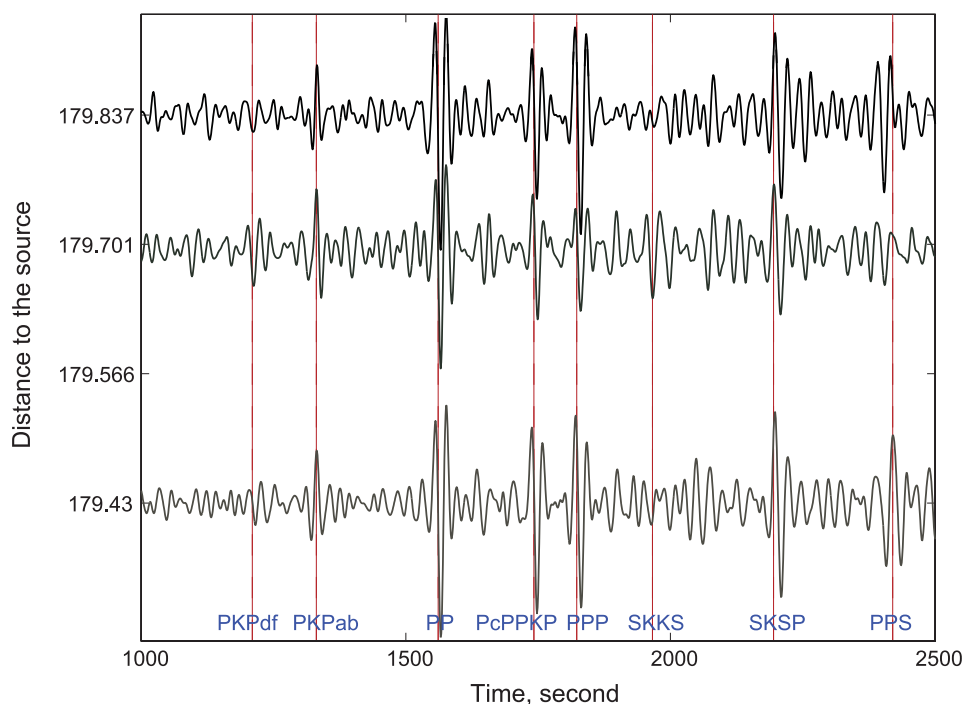


Figure 3. Vertical component seismograms of the three stations closest to the antipode of the event bandpassed between 20 and 50.

signal-to-noise ratio. For each distance bin between 166° and 180° , the signals are averaged over all azimuths to increase the coherent amplitudes due to the earthquake and reduce potential noise. This averaging also suppresses the azimuthal variability, which we do not study.

We then compare the observed signals with synthetic seismograms computed with AXISEM, a 2-D spectral-element solver for 3-D elastodynamics in global, spherically symmetric background models (Nissen-Meyer *et al.* 2007), using the isotropic version of the PREM model (Dziewonski & Anderson 1981) and including

viscoelastic attenuation. Results of this comparison are shown in Figs 4 and 5. The synthetics were computed using the global CMT focal mechanism and signals are generated at the same location as the USArray stations used and filtered in the same way as the USArray data, between 20 and 50 s. To focus on relative amplitudes between stations at different locations we normalized synthetics with a factor computed from amplitudes of the *PP* phase averaged over the five closest stations to the antipode. No time delay was applied. The signals are averaged over different distance bins similarly to the data (1° distance bins in Fig. 4 and 0.25° bins in Fig. 5).

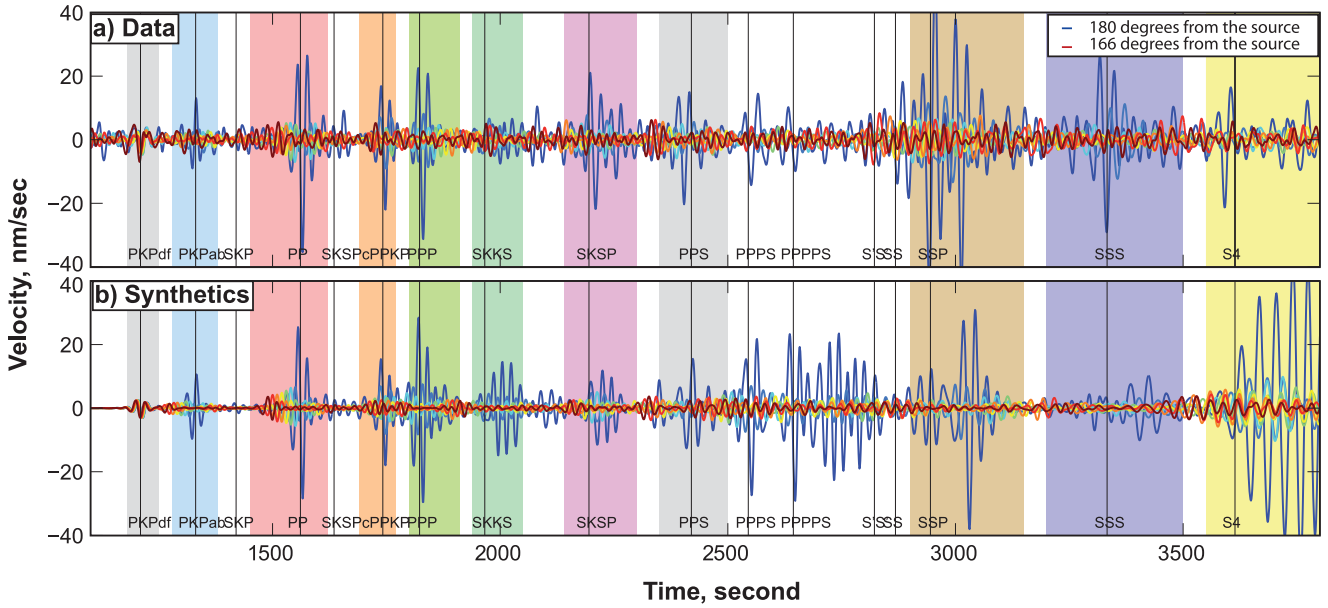


Figure 4. Vertical component seismograms bandpassed between 20 and 50 s and averaged in 1° distance bins. (a) Observations. (b) Synthetics. The colours of traces correspond to the distance from the source and evolve from red (166°) to blue (180°).

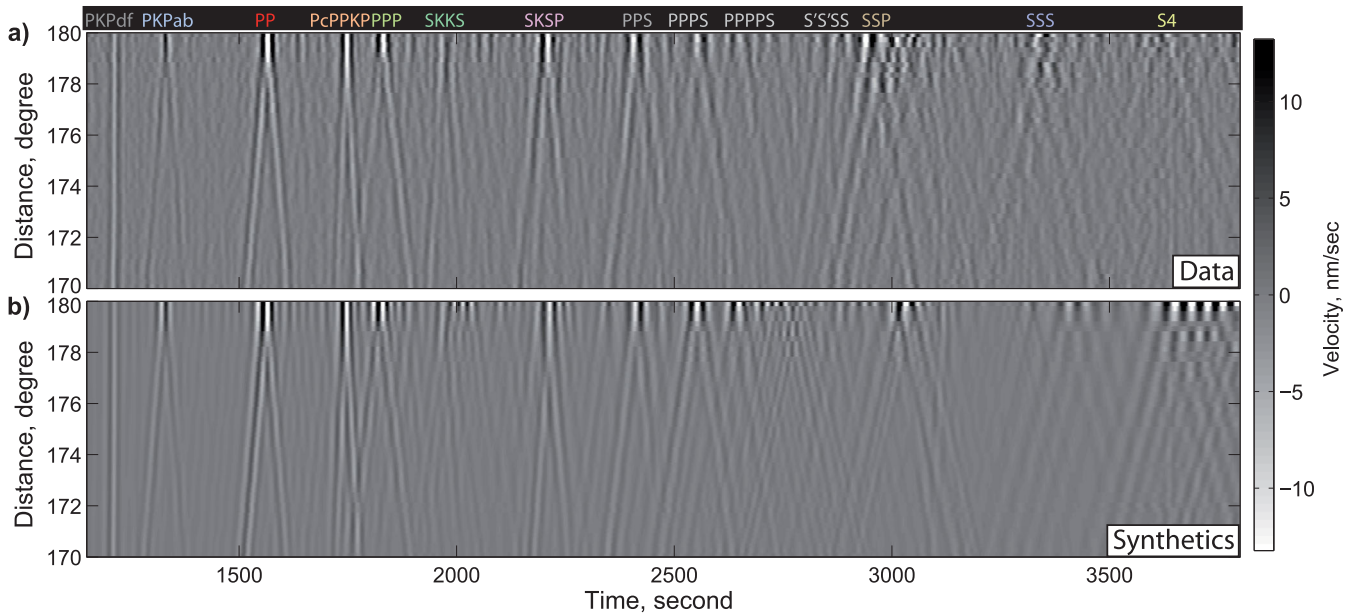


Figure 5. Time-distance gathers computed with averaging vertical-component seismograms in 0.25° bins. Signals were bandpassed between 20 and 50 s. (a) Observations. (b) Synthetics.

Similarly to what is predicted from numerical modelling, the observed *PKIKP* waves arrive nearly simultaneously and with same amplitudes at all stations (Figs 4 and 5). This is explained by the incident angle of the waves arriving from under the network (Fig. 2a). A further study is shown in Appendix A.

For all other body-wave phases, the amplification is clearly observed. Observations over long-range of epicentral distances allows us to identify the converging and diverging branches propagating below minor and major arcs, respectively (Fig. 2b).

4 OBSERVATION OF SPATIAL FOCUSING

In Fig. 4, a considerable difference in the amplitudes between the observed and the synthetic antipodal signals appears after 2500 s when the wavefield begins to be dominated by seismic waves reflected many times at the surface, which are strongly sensitive to the upper-mantle structure. Amplitude of the observed seismic waves might be decreased because of (1) combination of a possible incomplete intrinsic attenuation and (2) the scattering at the 3-D

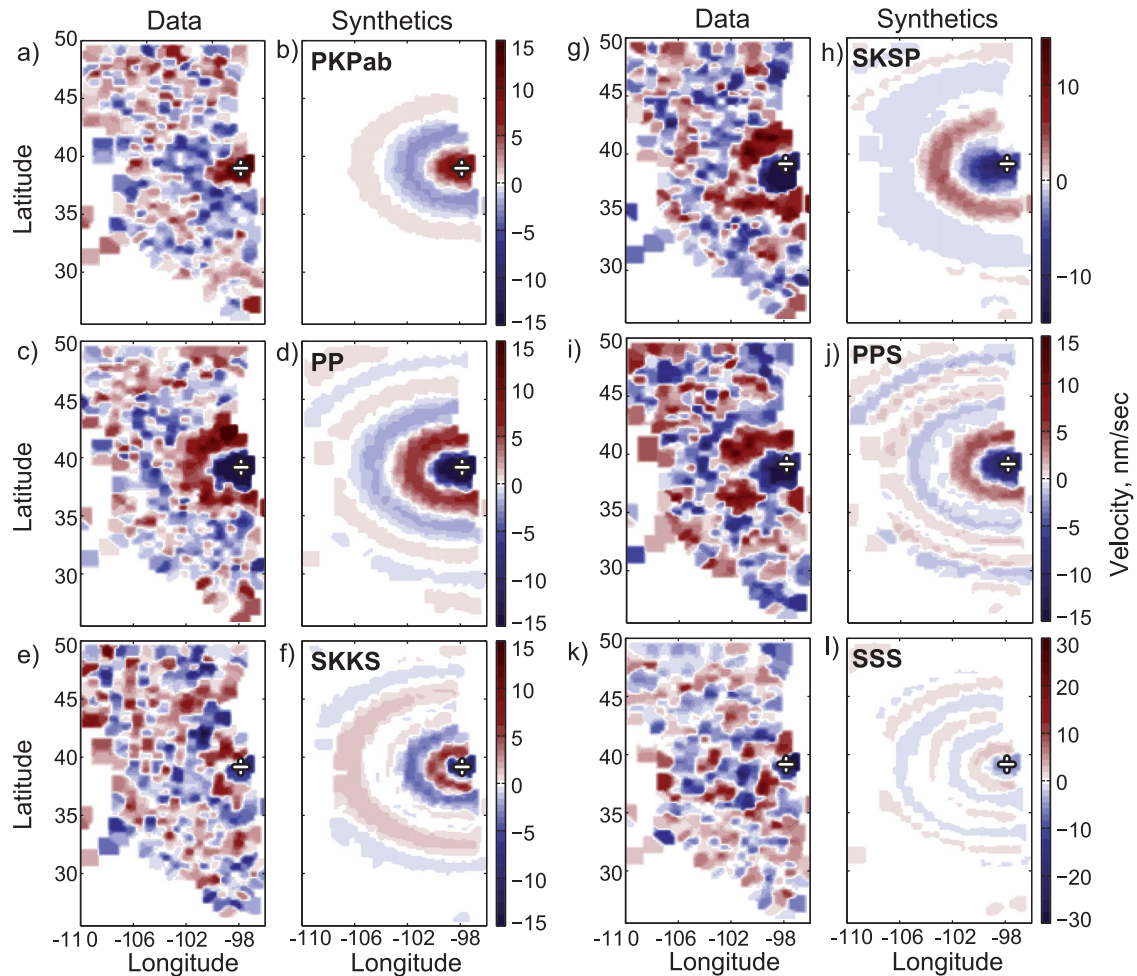


Figure 6. Spatial snapshots of the observed and synthetic velocity signals at the different stations at the time maximizing antipodal amplitude for *PKPab*, *PP*, *SKKS*, *SKSP*, *PPS* and *SSS*. We use the vertical component of the velocity signals bandpassed between 20 and 50 s.

heterogeneities, which are not considered in the synthetics. The effects of 3-D heterogeneities are more clearly revealed when analysing the spatial properties of the wavefield. Fig. 6 shows spatial snapshots of the observed and synthetic wavefields corresponding to times of maximum focusing (maximizing antipodal amplitude) of the different seismic phases: *PKPab* (*PKP*), *PP*, *SKKS*, *SKSP*, *PPS* and *SSS*.

These images are obtained by interpolating instantaneous values observed at individual stations at times of largest amplitude at the antipode for each phase. As a consequence, the signal-to-noise ratios are lower than those for stacked signals shown in Figs 4 and 5. Nevertheless, spatial patterns are clearly observed.

The observed patterns are compared to those obtained from synthetic seismograms computed with the source mechanism from the Global CMT catalogue. For the phases represented, the antipodal focusing results in interferometric patterns. When the waves are well focused, this pattern has a concentric structure with a main maximum coinciding with the position of the antipode as illustrated by predictions from synthetic seismograms (*PKPab* and *PP* phases in Figs 6a,b and 6c,d, respectively). Despite the low signal-to-noise ratios, clear interferometric patterns can be seen in the observations for most of *P* waves with the main maxima similar in size and position to those predicted for the spherically symmetrical Earth's model. In the best cases, a few secondary maxima can be recognized, as illustrated in Figs 6(c) and (d) for the *PP* phase. The patterns are

quite consistent between the data and the synthetics with the same wavelength of the concentric circular structures and a focusing at the antipode.

The signal-to-noise ratio decreases for later arriving phases such as *SKKS* (Figs 6e and f). The observed interferometric patterns start to deviate from the predicted ones for the converted phases like *SKSP* or *PPS* (Figs 6g,h or 6i,j). The focusing deviates from the antipode and the patterns do not look circular anymore.

The observed interferometric patterns become strongly irregular and differ from the synthetic data for the multiply reflected *S* waves (Figs 6k and l), indicating that the 3-D heterogeneity deteriorates the focusing of these waves mainly propagating in the upper mantle.

5 BEAMFORMING ANALYSIS

Fig. 2 shows the ray paths for different phases focusing at the antipode. In a perfectly spherically symmetrical structure, waves arrive simultaneously from all directions and focus exactly at the antipode. As a consequence of the 3-D heterogeneity in the Earth, waves coming to the antipode from different directions do not arrive exactly simultaneously. These differences in traveltimes of waves coming from different directions distort the perfect focusing and, if sufficiently strong, may even shift the main focusing point away from antipode. Appendix B studies the possibility that this deviation is linked to the focal mechanism of the fault.

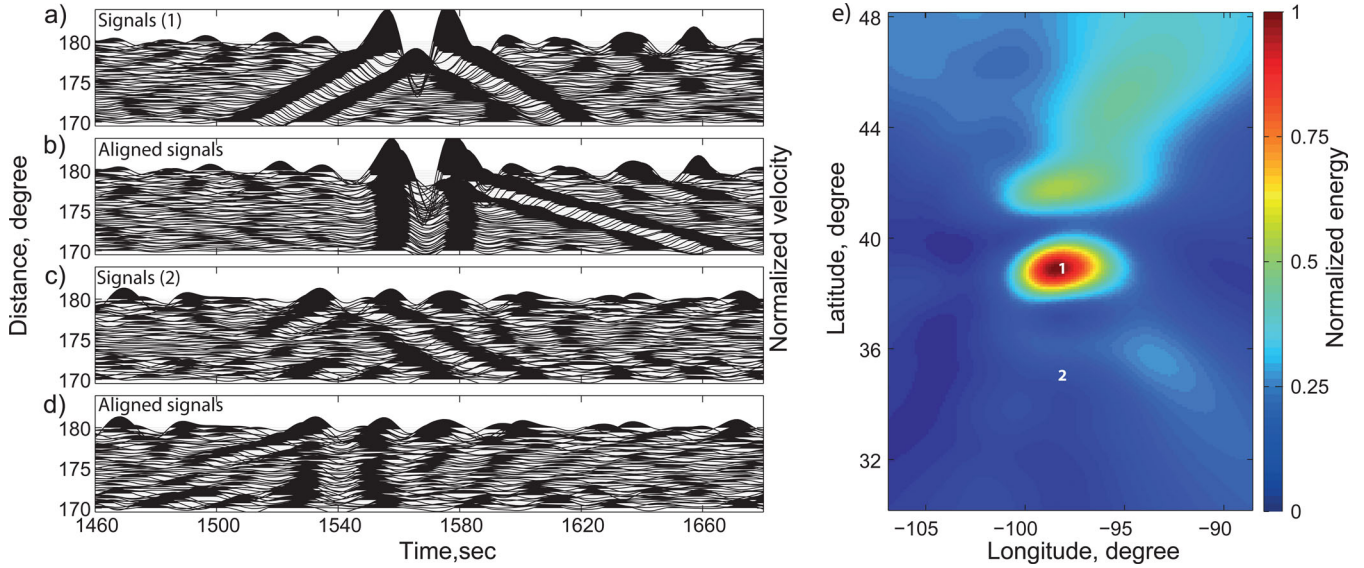


Figure 7. (a) Seismograms bandpassed between 20 and 50 s, stacked in 1° bins, and aligned with respect to distances to the epicentre's antipode. (b) Similar to (a) after applying a moveout correction with a slowness of *PP* waves propagating along the minor arc. (c) Similar to (a) but aligned with respect to point 2. (d) Similar to (c) and after applying a moveout correction maximizing the function from eq. (3). (e) Normalized beamforming result obtained from eq. (2) over an area around the antipode for the minor waves of *PP*. White numbers indicate positions of points 1 and 2 discussed in the text.

We apply a beamforming analysis to define the location of strongest focusing.

For this goal, we do not use the most standard 'plane-wave' beamforming algorithm but a version where the traveltimes shifts are computed with assuming a particular location of a focusing point.

We assume that this location may be different for different seismic phases. We also consider that at the scale of the array used, each phase is propagating as converging or diverging cylindrical waves with a constant slowness. Based on these assumptions, we test different positions R and apparent slownesses s and we construct the following beamforming operator:

$$B(R, s) = \int_{\omega_1}^{\omega_2} \left| \frac{1}{N_s} \sum_{n=1}^{N_s} U_n(\omega) e^{-i\omega dt(R, r_n, s)} \right| d\omega, \quad (1)$$

where: $dt(R, r_n, s) = \text{dist}(R, r_n)s$ are the time delays expected for a wave converging to a point R with a slowness s and $\text{dist}(R, r_n)$ is the distance between the station r_n and the point R . U_n is the Fourier transform of the station n . N_s is the number of stations and ω_1 and ω_2 define the range of frequencies used for the analysis (the period are 20–50 s in our case).

The beamforming operator (1) formulated in frequency domain is equivalent to a sequence of three operations in time domain: (1) alignment of signals relative to a tested focal point, (2) shifting of signals assuming a constant slowness and (3) stacking. Application of the beamforming analysis to the *PP* waves is illustrated in Fig. 7. When we consider the antipode as a main focusing point (point 1 in Fig. 7e), the signals are well aligned and clearly show the minor and major waves (Fig. 7a). After applying time-shifts based on theoretical slowness of *PP* waves (Fig. 7b), converging waves arrive simultaneously and the resulting stack is very strong (Fig. 7c). When we test a position away from the antipode (Figs 7c and d, position 2 in Fig. 7e), the alignment and stacking are significantly deteriorated.

For a wavefield composed of a single converging wave, the function $B(R, s)$ should have a single maximum $[R_{\max}, s_{\max}]$ with R_{\max} giving the location of the focusing and s_{\max} the wave slowness. If

more than one wave is present in the analysed records, the function $B(R, s)$ may contain several distinct maxima. For most phases (except the *PKIKP*) we see distinct maxima for waves propagating along minor and major arcs. For the graphical representations, we define the following functions:

$$B_R(R) = \int_{s_{\max} - \delta s}^{s_{\max} + \delta s} B(R, s) ds \quad (2)$$

and

$$B_s(s) = \iint_{\delta x \delta y} B(R, s) dx dy, \quad (3)$$

Intervals δs and $\delta x \delta y$ are selected to emphasize the part of the distribution close to the maxima of for the slowness or of the focusing location.

The geometry of the stations is not regular around the antipode of the earthquake with most of them located to the West (Fig. 1). This one-sided distribution may bias the shape of focusing determined with the beamforming analysis. To check this, we systematically tested the beamforming with a group of synthetic seismograms generated for stations homogeneously distributed around the antipode in addition to the analysis with real station locations (Appendix C). There results do not show significant variations compared to the results using the USArray locations.

6 DISCUSSION

Figs 8–13 show results of the beamforming analysis for several phases: *PKPab*, *PP*, *SKKS*, *SKSP*, *PPS* and *SSS* (see Fig. 2a for corresponding rays).

We observe a robust focusing for the main *P*-wave phase: *PKPab* (Figs 6a and 8) and *PP* (Figs 6c and 9), for both the minor and the major arc propagations (Fig. 2b).

The main observed focal spot is very close to the prediction from PREM in terms of its location and spatial extent for *PP*, the phase with highest amplitude. The energy of the *PP* waves is well focused at the antipode position (Fig. 9). The slowness observed

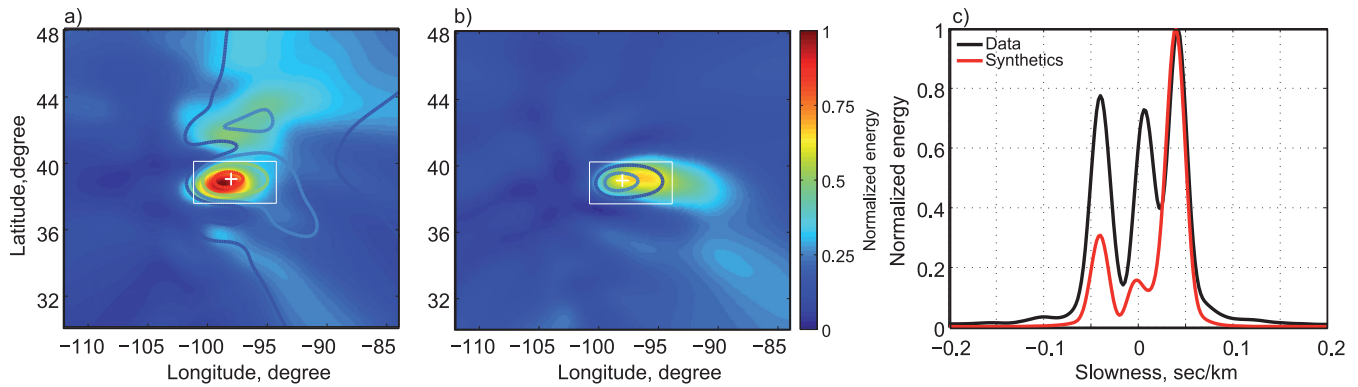


Figure 8. Results of the beamforming for the phases *PKPab*. (a) Energy B_R for the waves propagating along the minor arc and integrated in the slowness interval $\delta s = [0.03 \ 0.05] \text{ s km}^{-1}$. The observations are represented as a colourmap and the synthetics with coloured lines. The energy is normalized for the synthetics and data separately for an easier comparison. The white cross shows the earthquake's antipode. (b) Energy B_R for the waves propagating along the major arc ($\delta s = [-0.05 \ -0.03] \text{ s km}^{-1}$). (c) Energy B_s around main focusing locations $\delta x \delta y$ (shown with the grey rectangles in a, b).

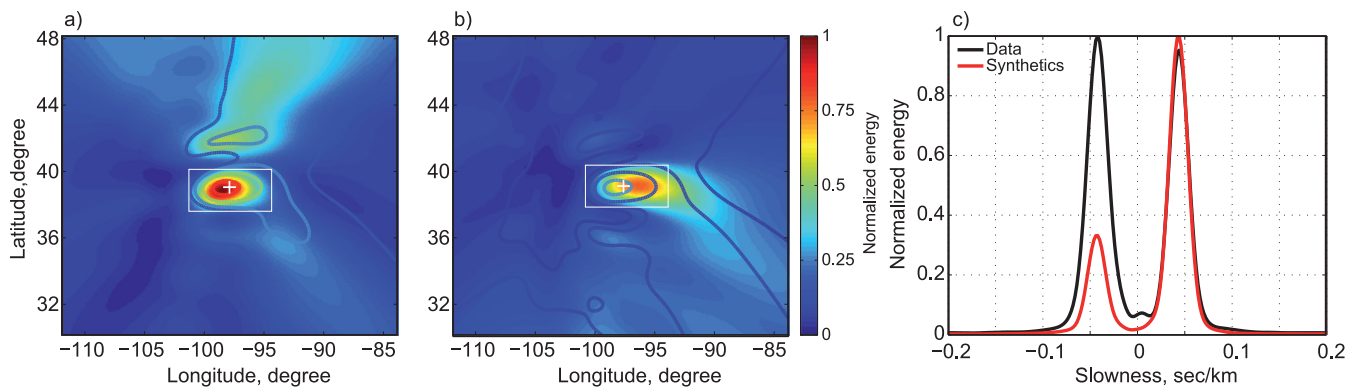


Figure 9. Results of the beamforming for the phases *PP*. (a) Energy B_R for the waves propagating along the minor arc and integrated in the slowness interval $\delta s = [0.035 \ 0.055] \text{ s km}^{-1}$. The observations are represented as a colourmap and the synthetics with coloured lines. The energy is normalized for the synthetics and data separately for an easier comparison. The white cross shows the earthquake's antipode. (b) Energy B_R for the waves propagating along the major arc ($\delta s = [-0.055 \ -0.035] \text{ s km}^{-1}$). (c) Energy B_s around main focusing locations $\delta x \delta y$ (shown with the grey rectangles in a, b).

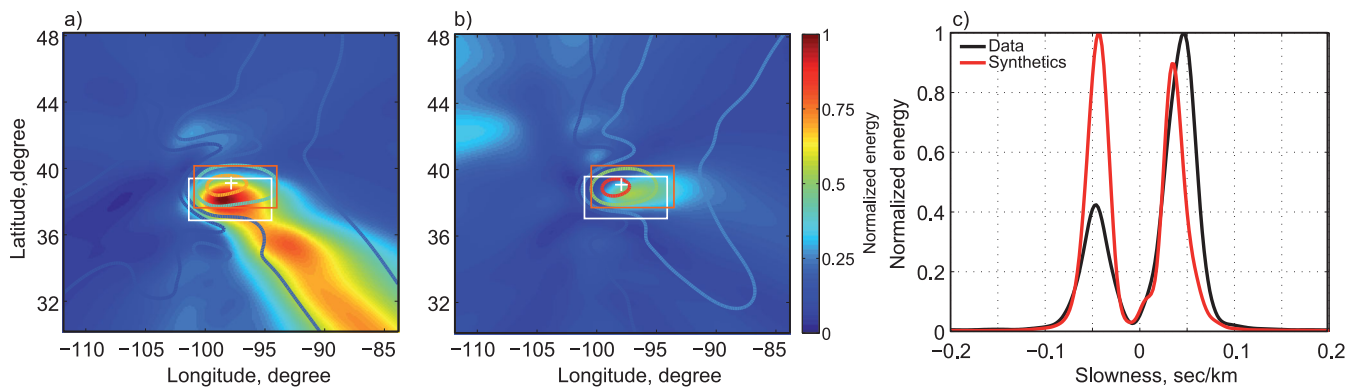


Figure 10. Results of the beamforming for the phases *SKSP*. (a) Energy B_R for the waves propagating along the minor arc and integrated in the slowness interval $\delta s = [0.035 \ 0.065] \text{ s km}^{-1}$ for the observations and $\delta s = [0.025 \ 0.05] \text{ s km}^{-1}$ for the synthetics. The observations are represented as a colourmap and the synthetics with coloured lines. The energy is normalized for the synthetics and the data separately for an easier comparison. (b) Energy B_R for the waves propagating along the major arc ($\delta s = [-0.065 \ -0.035] \text{ s km}^{-1}$ for the observations and $\delta s = [-0.05 \ -0.025] \text{ s km}^{-1}$ for the synthetics). (c) Energy B_s around main focusing locations $\delta x \delta y$ (shown with the grey rectangles for the observations and orange rectangles for the synthetics in a, b).

at the antipode (after averaging over the main focalization zone) is of 0.045 s km^{-1} for the waves propagating along the minor arc and -0.045 for the ones propagating along the major arc (Fig. 9c) which is very close to predictions estimated by global traveltime tables (Buland & Chapman 1983). The main difference between

the observations and the synthetics is the ratio of amplitude of the beamforming energy between the minor and major arc propagations. Similarly, the *PKPab* phase (Fig. 8) shows a good focusing at the antipode and a good match between the observed and the predicted major slownesses.

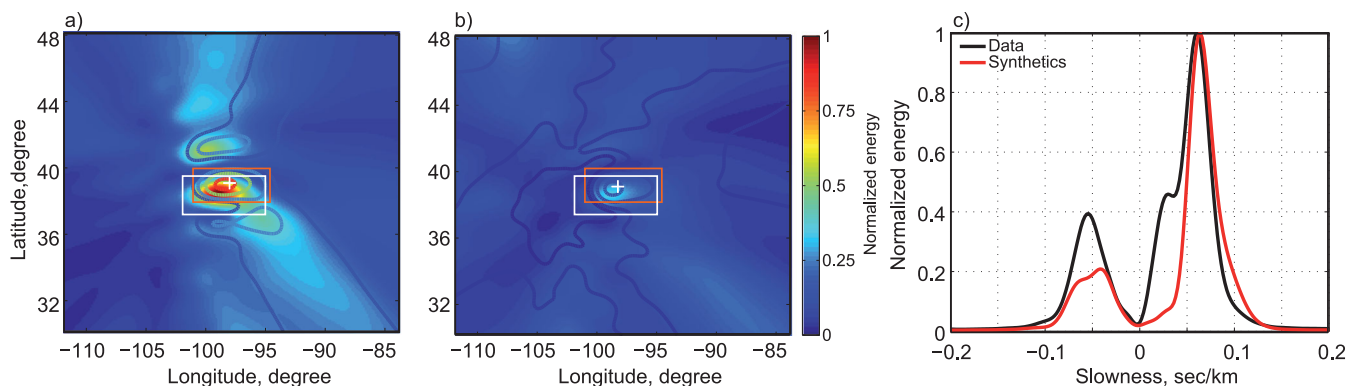


Figure 11. Results of the beamforming for the phases *PPS*. (a) Energy B_R for the waves propagating along the minor arc and integrated in the slowness interval $\delta s = [0.045 \text{ } 0.075] \text{ s km}^{-1}$ for the observations and $\delta s = [0.05 \text{ } 0.08] \text{ s km}^{-1}$ for the synthetics. The observations are represented as a colourmap and the synthetics with coloured lines. The energy is normalized for the synthetics and the data separately for an easier comparison. (b) Energy B_R for the waves propagating along the major arc ($\delta s = [-0.075 \text{ } -0.045] \text{ s km}^{-1}$ for the observations and $\delta s = [-0.08 \text{ } -0.05] \text{ s km}^{-1}$ for the synthetics). (c) Energy B_s around main focusing locations $\delta x \delta y$ (shown with the grey rectangles for the observations and orange rectangles for the synthetics in a, b).

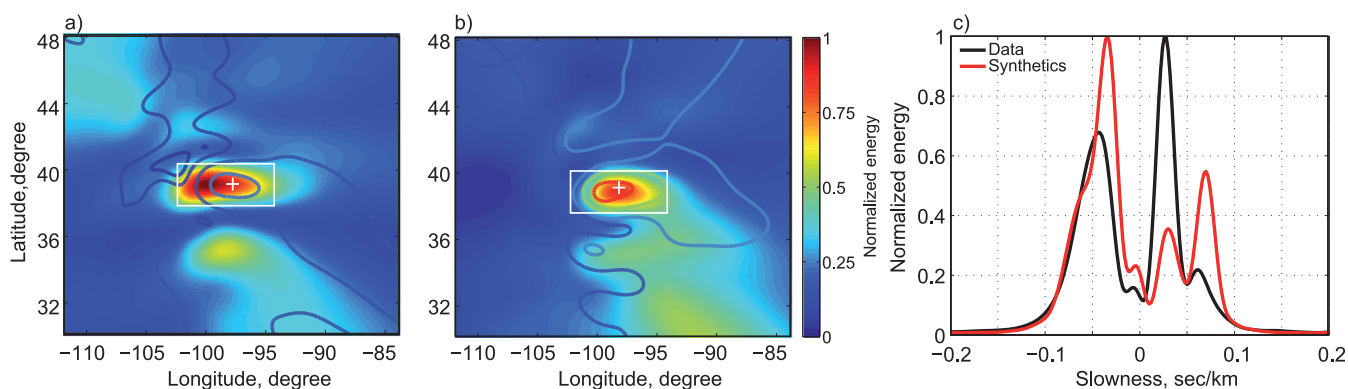


Figure 12. Results of the beamforming for the phases *SKKS*. (a) Energy B_R for the waves propagating along the minor arc and integrated in the slowness interval $\delta s = [0.02 \text{ } 0.05] \text{ s km}^{-1}$ for the observations and synthetics. The observations are represented as a colourmap and the synthetics with coloured lines. The energy is normalized for the synthetics and the data separately for an easier comparison. (b) Energy B_R for the waves propagating along the major arc ($\delta s = [-0.05 \text{ } -0.02] \text{ s km}^{-1}$ for the observations and synthetics). (c) Energy B_s around main focusing locations $\delta x \delta y$ (shown with the grey rectangles in a, b).

For the phase *SKSP*, the observed focusing significantly differs from the synthetic prediction. In the spatial snapshot representation and in the beamforming results (Figs 6g and 10a), a decay of about 115 km to the south is observed between the energy focusing of the observations and synthetics. The maximum slowness observed with the data is 0.05 s km^{-1} , while the value predicted with synthetic seismograms is 0.035 s km^{-1} . A similar southward shift of the main focusing position is observed for another converted phase *PPS* (Fig. 11). In contrast, the phase *SKKS* does not exhibit the southward shift of the main focusing location (Fig. 12) though it seems disturbed by the previous arrivals and shows a low signal-to-noise ratio (Fig. 4).

The observed focusing becomes very disturbed for the multiple *S* waves: *SSP*, *SSS*, *SSSS* ... (Figs 6d and 13). The energy is still amplified when closer to the antipode, but the main focusing spot is badly defined for the data when compared with the synthetics. This observation confirms the strong influence of the upper mantle *S* velocity heterogeneity on the defocusing of the antipodal phases.

The southward shift of the main focus point that is not systematically observed in all phases is difficult to explain by an effect of focal mechanism. First, the mechanism from the Global CMT catalogue has a dip close to 45° and in this case the expected shifts are very small, as discussed in Appendix B. Nonetheless, a shift

caused by a very different mechanism than the Global CMT mechanism should imply similar behaviour for all phases generated as *P* or as *S* waves at the source of the event. Even so, the shift is only observed for some phases and not for others. Therefore, the most likely explanation is that this shift is caused by some large-scale heterogeneity within the Earth.

The most important southward shift of the focus point is observed for the *SKSP* phase. However, *PKPab* and another *S*-wave phase, *SKKS*, which both travel through the core, do not exhibit the same systematic variation. They all travel through the core, but *SKSP* waves bounce one time at the surface, indicating that the heterogeneity is located in the mantle or the crust rather than in the core.

The first *P*-wave phases focus at the antipode and do not show this shift but there are deteriorations later in the signals. Indeed no shift is observed for *PP* and *PKPPcP*. However, *PPP* and *PPS* are shifted, meaning that shifts can be the consequence of multiple bounces.

These variations of focusing could be linked to the different travelpaths of the waves arriving at the antipode from the south or the north. Waves travelling to the antipode from the north bounce mostly in the continental crust of Eurasia, while waves travelling from south bounce mostly within the oceanic crust. The differences

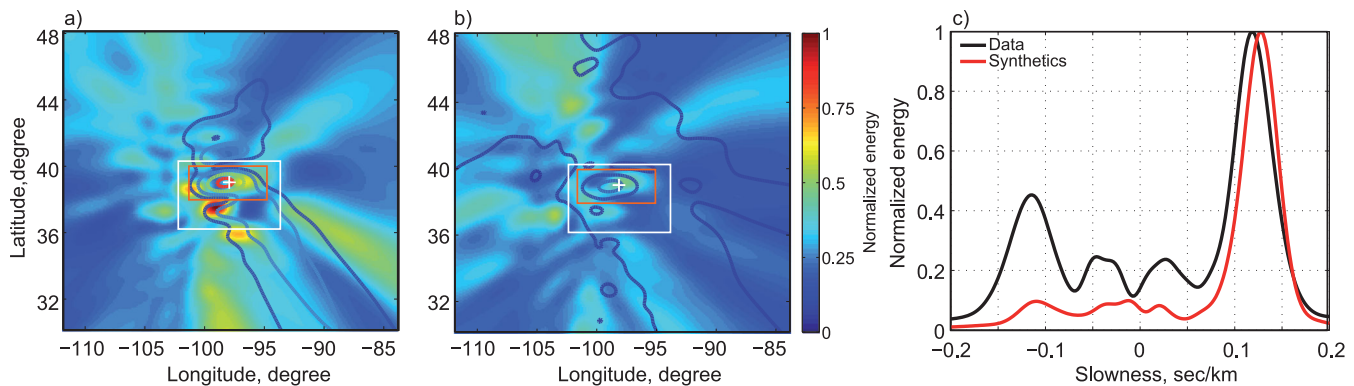


Figure 13. Results of the beamforming for the phases SSS. (a) Energy B_R for the waves propagating along the minor arc and integrated in the slowness interval $\delta s = [0.095 \text{ } 0.145] \text{ s km}^{-1}$ for the observations and $\delta s = [0.105 \text{ } 0.15] \text{ s km}^{-1}$ for the synthetics. The observations are represented as a colourmap and the synthetics with coloured lines. The energy is normalized for the synthetics and data separately for an easier comparison. (b) Energy B_R for the waves propagating along the major arc ($\delta s = [-0.145 \text{ } -0.095] \text{ s km}^{-1}$ for the observations and $\delta s = [-0.15 \text{ } -0.105] \text{ s km}^{-1}$ for the synthetics). (c) Energy around main focusing locations $\delta x \delta y$ (shown with the grey rectangles for the observations and orange rectangles for the synthetics in a, b).

in crustal thickness or the differences of mantle and crust composition in oceanic or continental contexts might induce time delays or changes in the shapes of the waveforms, perhaps implying signal interference, changing the focusing of the waves.

ACKNOWLEDGEMENTS

We thank Matthieu Landes for fruitful discussions. We thank Alexandre Fournier and Tarje Nissen-Meyer for their help on the computing of synthetics with Axisem. Data from the TA network are made freely available as part of the EarthScope US-Array facility, operated by Incorporated Research Institutions for Seismology (IRIS). This work was supported by the Commissariat à l’Energie Atomique (CEA, France) and by the European Research Council under the contract FP7 ERC Advanced grant 227507 (WHISPER).

REFERENCES

- Aki, K. & Richards, P.G., 1980. *Quantitative Seismology: Theory and Methods*, Vol. 1, WH Freeman and Co.
- Buland, R. & Chapman, C., 1983. The computation of seismic travel times, *Bull. seism. Soc. Am.*, **73**(5), 1271–1302.
- Butler, R. & Tsuboi, S., 2010. Antipodal seismic observations of temporal and global variation at Earth’s innerouter core boundary, *Geophys. Res. Lett.*, **37**(11), L11301, doi:10.1029/2010GL042908.
- Butler, R., Brocher, T.M. & Rial, J.A., 1986. Inner Core Experiments: teleseismic exploration of the antipode, *EOS, Trans. Am. geophys. Un.*, **67**(8), 89.
- Cormier, V.F. & Stroujkova, A., 2005. Waveform search for the innermost inner core, *Earth planet. Sci. Lett.*, **236**(1–2), 96–105.
- Crotwell, H., Owens, T. & J, R., 1999. The TauP Toolkit: flexible seismic travel-time and ray-path utilities, *Seismol. Res. Lett.*, **70**, 154–160.
- Dziewonski, A. & Anderson, D., 1981. Preliminary reference Earth model, *Phys. Earth planet. Inter.*, **25**, 297–356.
- Ekström, G., Nettles, M. & Dziewonski, A., 2012. The global CMT project 2004–2010: centroid-moment tensors for 13,017 earthquakes, *Phys. Earth planet. Inter.*, **200–201**, 1–9.
- Lin, F.-C. & Tsai, V.C., 2013. Seismic interferometry with antipodal station pairs, *Geophys. Res. Lett.*, **40**(17), 4609–4613.
- Meschede, M.A., Myhrvold, C.L. & Tromp, J., 2011. Antipodal focusing of seismic waves due to large meteorite impacts on Earth, *Geophys. J. Int.*, **187**(1), 529–537.

- Nissen-Meyer, T., Fournier, A. & Dahlen, F.A., 2007. A two-dimensional spectral-element method for computing spherical-earth seismograms—I. Moment-tensor source, *Geophys. J. Int.*, **168**(3), 1067–1092.
- Niu, F. & Chen, Q.-F., 2008. Seismic evidence for distinct anisotropy in the innermost inner core, *Nat. Geosci.*, **1**(10), 692–696.
- Poupinet, G., Souriau, a. & Jenatton, L., 1993. A test on the Earth’s core-mantle boundary structure with antipodal data: example of Fiji-Tonga earthquakes recorded in Tamanrasset, Algeria, *Geophys. J. Int.*, **113**(3), 684–692.
- Rial, J., 1978. On the focusing of seismic body waves at the epicentre’s antipode, *Geophys. J. R. astr. Soc.*, **55**, 737–743.
- Rial, J.A. & Cormier, V.F., 1980. Seismic waves at the epicenter’s antipode, *J. geophys. Res.*, **85**(80), 2661–2668.
- Sun, X. & Song, X., 2002. PKP travel times at near antipodal distances: implications for inner core anisotropy and lowermost mantle structure, *Earth planet. Sci. Lett.*, **199**, 429–445.

APPENDIX A: OBSERVATION OF PKIKP BEHAVIOUR

Phase *PKIKP* shows a different behaviour from the other phases because of the arrival of the waves from right under the network (Fig. 2a). This implies that the waves arrive at the same time at the different stations of the network (Figs 4 and 5) and thus do not interfere into a focalization effect.

Spatial snapshots are performed to show this behaviour, using the same method as in Section 4. As expected, the amplitude of the *PKIKP* waves is constant over the whole network (Fig. A1) for the data and synthetics, showing the simultaneous arrivals of the *PKIKP* waves.

Furthermore, beamforming analysis, discussed in Section 6, shows this effect too. No strong focusing is observed for the *PKIKP* wave (Fig. A2), which agrees with the simultaneous arrival time of the signal at all stations (seen on Figs 4 and 5). This behaviour is predicted by synthetic seismograms and is well seen in the data, despite the low signal-to-noise ratio (Fig. A1). The most efficient slowness obtained for this phase is around zero implying an almost vertical incidence of this wave at the antipode explained by its travelpath (Fig. 2a).

PKIKP is the only phase showing this behaviour because it is the only one travelling directly from the source to the network with no refraction or reflection at the different interfaces of the earth. It gives a direct view of the event and the earth travelled without interferences between the arrivals.

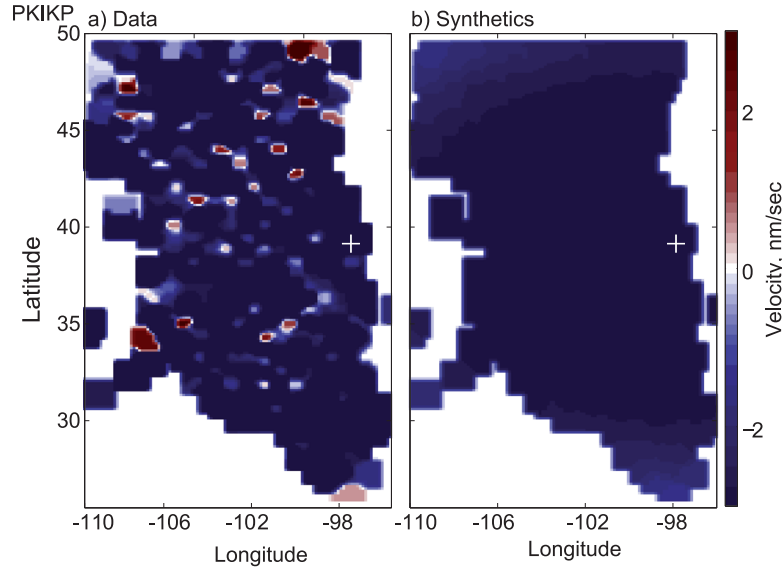


Figure A1. Spatial snapshots of the observed and synthetic velocity signals at the different stations at the time maximizing antipodal amplitude for *PKIKP*. We use the vertical component of the velocity signals bandpassed between 20 and 50 s.

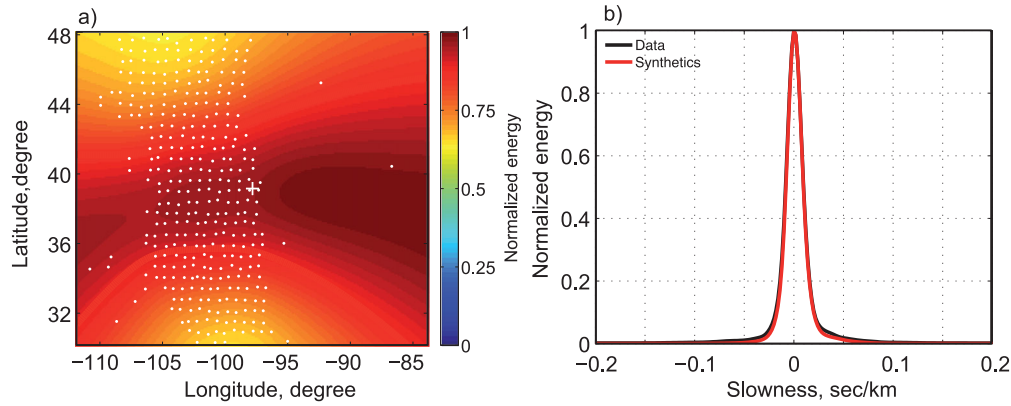


Figure A2. Results of the beamforming for the phase *PKIKP*. (a) Energy B_R integrated in the slowness interval $\delta s = [-0.01 \ 0.01] \text{ s km}^{-1}$. The observations are represented as a colourmap and the synthetics with coloured lines. The energy is normalized for the synthetics and data separately for an easier comparison. The locations of the stations are represented with the black points. (b) The energy B_s computed over the all area since no focusing is observed.

APPENDIX B: INFLUENCE OF THE EARTHQUAKE FOCAL MECHANISM ON THE ANTIPODAL AMPLIFICATIONS

Antipodal amplification is due to constructive interferences of waves arriving at the antipode from different directions. This interference may be partially damaged if waves coming from different azimuth do not arrive exactly in phase. One possible cause for such decorrelation might be the influence of the 3-D heterogeneity within the Earth. Therefore, observing the deviation of the antipodal amplification and focusing from predictions in the spherically symmetric models could help quantify the degree of the Earth's heterogeneity. Another possible cause of non-perfect antipodal focusing might be the influence of the source radiation pattern.

The influence of focal mechanism was tested with synthetic seismograms. 625 synthetic signals are generated for virtual stations disposed uniformly around the antipode with distances from 174° to 180° to the source of the earthquake (Fig. A3c). The synthetics are filtered using a Butterworth bandpass filter between 20 and 50 s. Different earthquake mechanisms are tested (Figs A3a and b).

The strike and rake are constant with a value of 90° while the dip varies from 0° to 45° . For mechanisms with nearly vertical or nearly horizontal fault planes, vertical-component seismograms have low amplitudes for both *P* and *S* waves at antipodal stations. The reason for this is that the antipode coincides with the minima of the *P*-waves radiation pattern while most of the radiated *S*-waves energy propagates along horizontal components. For such mechanisms, the maximum of energy is shifted from the antipode (Fig. A4).

The far-field radiation patterns are computed for *P* and *S* waves generated by a point source at 12 km depth (Aki & Richards 1980). The radiation patterns in dimensionless form F^P and F^{SV} are given by:

$$\begin{aligned}
 F^P = & \cos \lambda \sin \delta \sin^2 i_e \sin 2(\phi - \phi_S) \\
 & - \cos \lambda \cos \delta \sin 2i_e \cos(\phi - \phi_S) \\
 & + \sin \lambda \sin 2\delta (\cos^2 i_e - \sin^2 i_e \sin^2(\phi - \phi_S)) \\
 & + \sin \lambda \cos 2\delta \sin^2 i_e \sin(\phi - \phi_S),
 \end{aligned} \tag{B1}$$

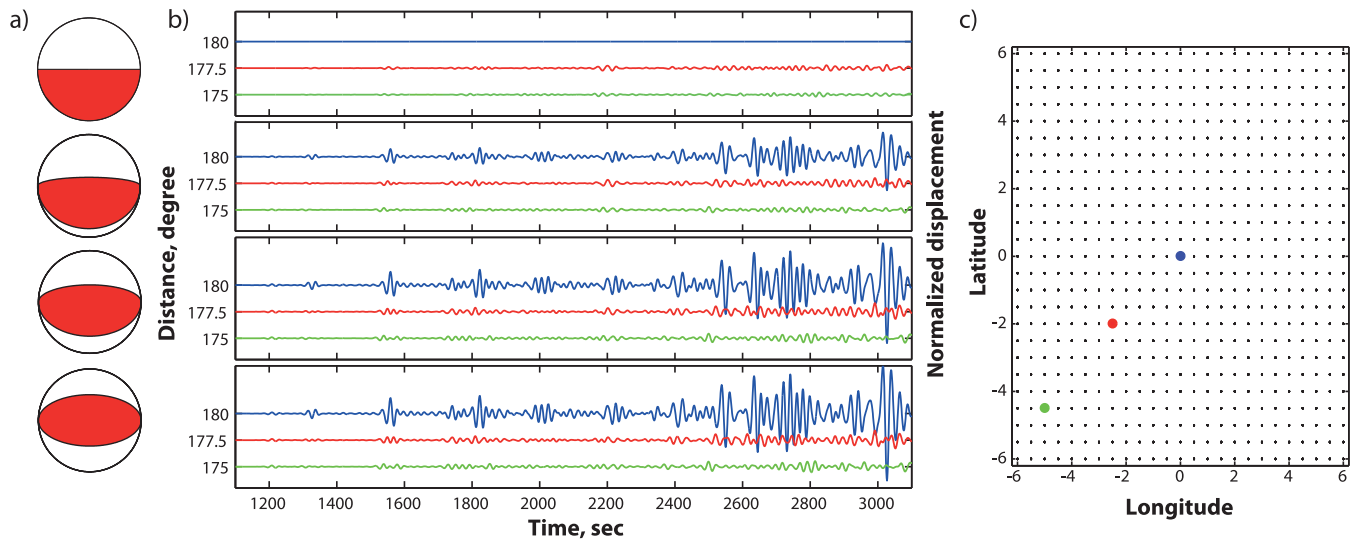


Figure A3. (a) The different tested focal mechanisms are plotted on the left-hand side of the figure. The strike and rake are constant with a value of 90° . The dip varies from 0° to 45° (by steps of 15°). (b) Synthetic displacement seismograms computed at near antipodal stations. The signals are filtered using a Butterworth bandpass filter between 20 and 50 s. The signals are drawn for three stations (plotted in c) at 175° , 177.5° and 180° of distance from the source (green, red and blue traces, respectively). (c) The different locations of the computed signals (175° , 177.5° and 180° in black, red and blue). Position (0,0) is the antipode of the source.

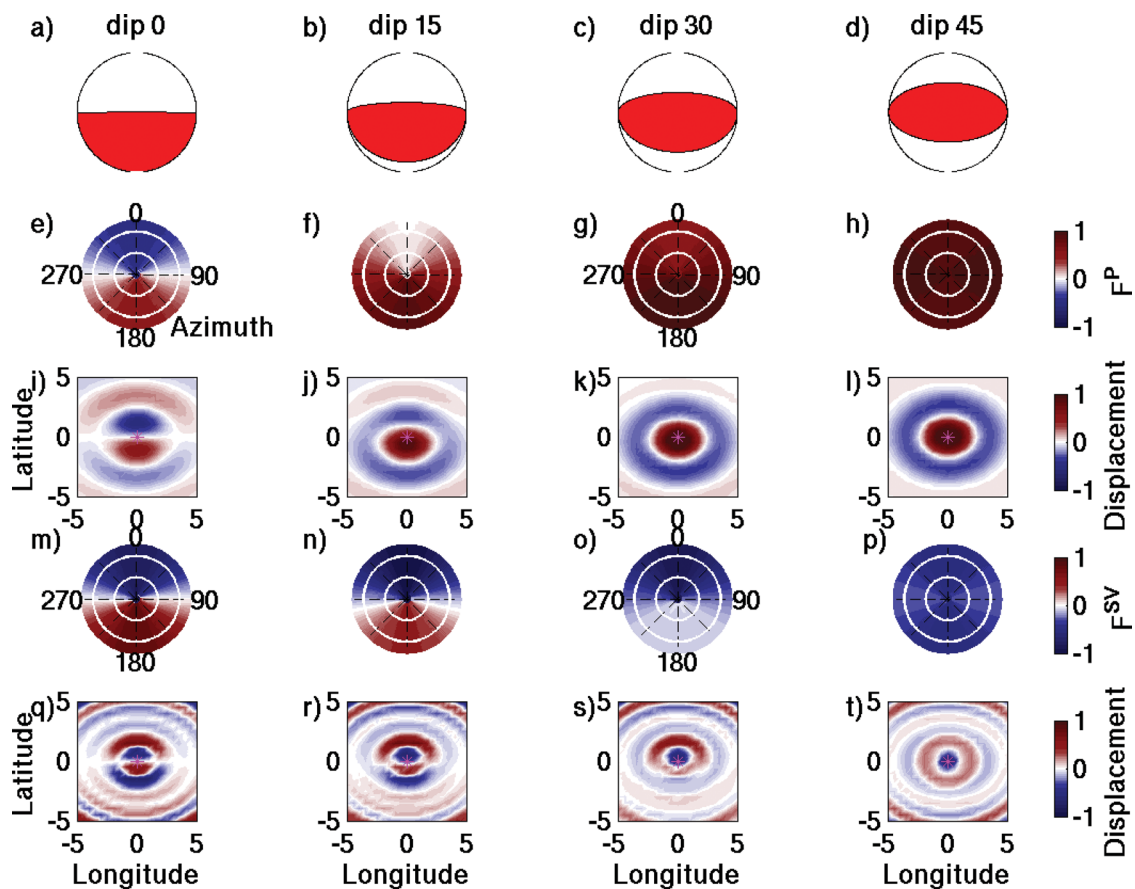


Figure A4. (a) The different focal mechanisms tested. The strike and rake are constant with a value of 90° . The dip varies from 0° to 45° . (b) Radiation patterns of the PP phase computed from (1) and shown in polar coordinates centred at the antipode position and distances varying between 174° and 180° . The white circles represent the distances to the source 175° and 177.5° . (c) Normalized vertical displacement for PP phase at the time of largest amplitude at the antipode at different positions. The magenta star shows the antipode location. (d) Radiation patterns of the SS phase computed from (2) and shown in polar coordinates centred at the antipode position and distances varying between 174° to 180° . (e) Amplitude displacement for SS phase at the time of largest amplitude at the antipode at the different positions.

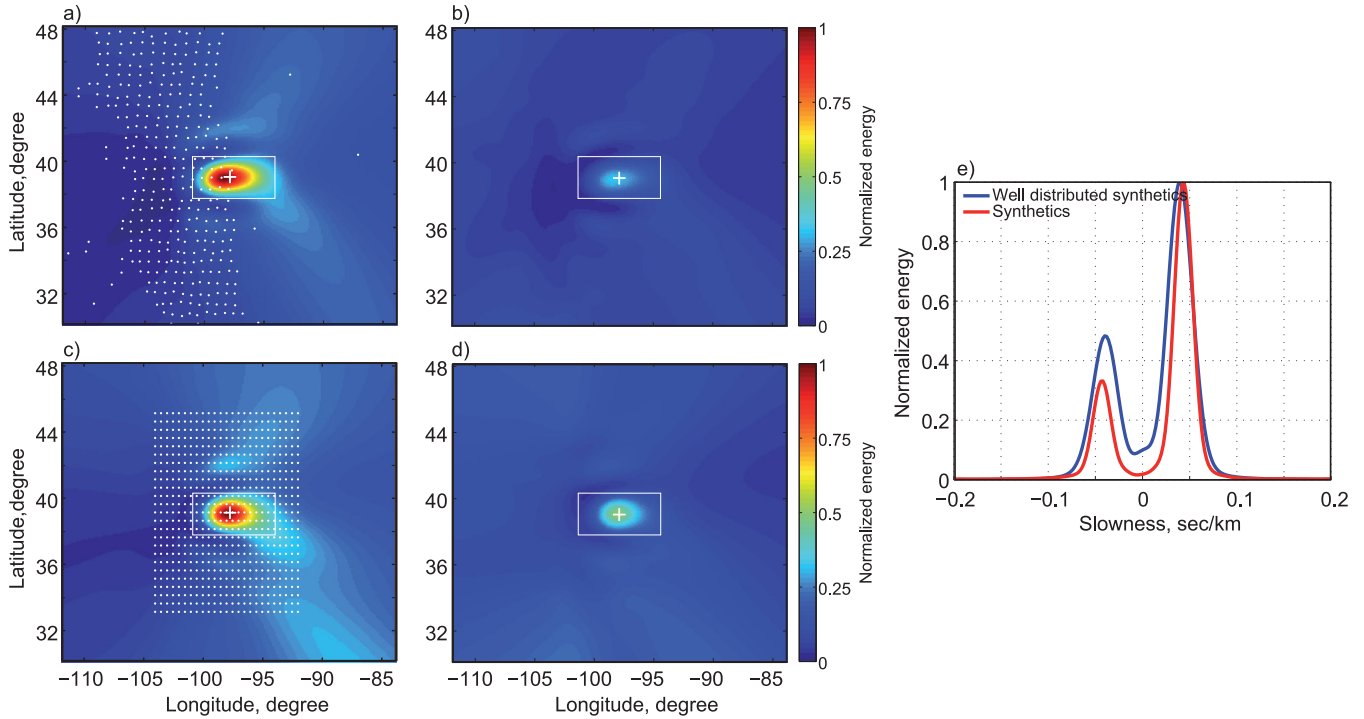


Figure A5. Results of the beamforming performed on synthetics for the phases *PP*. (a) Energy B_R for the waves propagating along the minor arc and integrated in the slowness interval $\delta s = [0.035 \ 0.055] \text{ s km}^{-1}$. The energy is normalized for the synthetics and data separately for an easier comparison. The white points show the location of the USArray station. (b) Energy B_R for the waves propagating along the major arc ($\delta s = [-0.055 \ -0.035] \text{ s km}^{-1}$). (c, d) Beamforming results computed from synthetic seismograms with a homogeneous distribution of stations. The white points represent the location of the well distributed stations. (e) Energy B_s around main focusing locations $\delta x \delta y$ (shown with the grey rectangles in a, b, c, d).

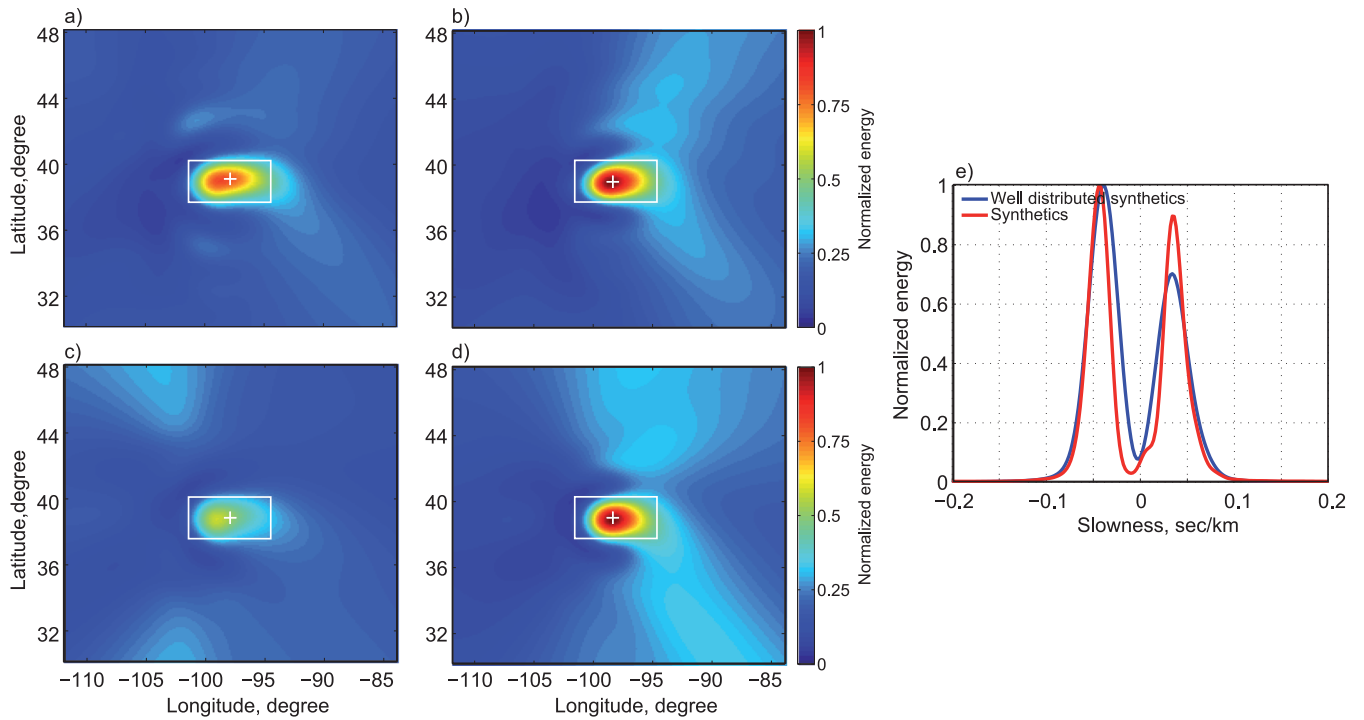


Figure A6. Results of the beamforming performed on the synthetics for the phases *SKSP*. (a) Energy B_R for the waves propagating along the minor arc and integrated in the slowness interval $\delta s = [0.025 \ 0.05] \text{ s km}^{-1}$. The observations are represented as a colourmap and the synthetics with coloured lines. The energy is normalized for the synthetics and data separately for an easier comparison. (b) Energy for the waves propagating along the major arc ($\delta s = [-0.05 \ -0.025] \text{ s km}^{-1}$). (c, d) Beamforming results computed from synthetic seismograms with a homogeneous distribution of stations. (e) Energy B_s around main focusing locations $\delta x \delta y$ (shown with the grey rectangles in a, b, c, d).

$$\begin{aligned}
F^{SV} = & \sin \lambda \cos 2\delta \cos 2i_e \sin(\phi - \phi_S) \\
& - \cos \lambda \cos \delta \cos 2i_e \cos(\phi - \phi_S) \\
& + \frac{1}{2} \cos \lambda \sin \delta \sin 2i_e \sin 2(\phi - \phi_S) \\
& - \frac{1}{2} \sin \lambda \sin 2\delta \sin 2i_e (1 + \sin^2(\phi - \phi_S)). \quad (B2)
\end{aligned}$$

ϕ_S , δ and λ are, respectively, the strike, dip and rake of the earthquake. i_e is its take-off angle and ϕ the source-receiver azimuth. Take-off angles for given epicentral distances are predicted by traveltimes and ray parameters calculator **ttimes** (Buland & Chapman 1983).

To interpret the observation made on vertical components, we use the F^P radiation pattern for P waves and F^{SV} radiation pattern for S waves (eqs B1 and B2, respectively). These radiation patterns are compared with amplitudes predicted by synthetic seismograms in Fig. A4. For a 45° dip fault the antipodal energy focusing is predicted for both PP and SS waves. With the variation of the dip from 45° to 0° , the locations of apparent focal points shift away from the antipode. The directions of these shifts are opposite for P

and S waves, which may lead to discrepancies in their maximum focusing positions.

APPENDIX C: BEAMFORMING RESULTS OBTAINED BY USING WELL DISTRIBUTED RECEIVERS

To observe the possible effect of the stations distribution in the beamforming results we performed the analysis explained in Section 6 on synthetics generated for a set of stations well-distributed around the antipode. Figs A5 and A6 give the results of the beamforming analysis for the synthetics generated at the location of USArray (a, b) and the synthetics generated using a set of well distributed stations around the antipode (c, d) for the phases PP and $SKSP$.

The results obtained with the beamforming method are similar when using synthetics generated with well-distributed stations or for the USArray locations. Still, some variations are observable, showing that the station distribution has some influence, but it does not influence the interpretations.